ROCK/FLUID INTERACTION BY INJECTION OF SUPERCRITICAL CO_2/H_2S: INVESTIGATION OF DRY-ZONE FORMATION NEAR THE INJECTION WELL

H. Ott[1,*], K. de Kloe[1], C. Taberner[1], F. Marcelis[1], Y. Wang[2], and A. Makurat[1]
Shell International Exploration and Production, (1) The Netherlands, (2) USA

This paper was prepared for presentation at the International Symposium of the Society of Core Analysts held in Halifax, Nova Scotia, Canada, 4-7 October, 2010

ABSTRACT

In the present paper we report on two consequences of formation dry-out due to the injection of dry or under-saturated acid-forming fluids such as CO_2 and H_2S into geological formations. The reported findings are coupled to each other and are relevant in the surrounding well-bore environment for CO_2 sequestration and acid-gas injection operations.

By injecting supercritical (SC) CO_2 into brine-saturated sandstone, we investigated salt precipitation due to drying in a capillary-pressure-dominated flow regime. Patterns of precipitated salt were observed along the flow direction as well as cross sectional patterns. A substantial impairment of the absolute permeability (K) was found but, despite high local salt accumulation, the effective CO_2 permeability ($K \cdot k_{rel}$) increased during the experiments.

In the second part of the paper we address the question of whether a dry zone is necessarily chemically stable. We injected SC H_2S into practically dry limestone. Substantial water production was observed as result of a dissolution reaction, which potentially prevents formation drying. The experiment demonstrates chemical rock/fluid interaction in the absence of an aqueous phase.

INTRODUCTION

The injection of CO_2 or acid gas into geological formations is a large-scale option for reducing anthropogenic greenhouse-gas emission (mainly CO_2) [1] and for disposal of contaminants from sour-gas production (mainly H_2S and CO_2) [2]. Deep saline aquifers and depleted hydrocarbon fields are potential subsurface deposits for these contaminants [1,2]. CO_2 and H_2S, however, interact chemically and physically with formation rock and, coupled with fluid flow and rock-mechanical strength, this creates uncertainties for sequestration projects. Some of these uncertainties concern the zone around the injection well where fluxes, concentrations and saturation gradients are highest. The injection of dry or under-saturated (with respect to water) fluids might even lead to formation dry-out, which causes dissolved salts to precipitate [3-7] and changes the chemical properties of the zone [8]. Here we present experimental results regarding these consequences, addressed by core-flood experiments on two distinctly different systems. The results also

show that chemical rock/fluid interaction and salt precipitation due to drying are ultimately connected to one another.

Initially, we investigated the drying process and the associated salt precipitation. Salt (mainly halite) precipitates as a result of the evaporation of formation water into the injected fluid. This process potentially impairs injectivity and has been investigated by several authors by means of numerical simulations and analytical models [3-7]. However, experimental data is scarce but crucial for injection operations, as several theoretical studies have shown that a modest reduction in porosity might lead to a serious reduction in permeability [9-12] and, hence, to a serious impairment of injectivity. Here, we aim to observe the effects of precipitation by evaporation only (as a physical process) and, hence, chemical rock-fluid interaction must be avoided. We injected SC CO_2 into brine-saturated sandstone, a combination that is supposed to be non reactive. During injection, the spatial and time evolution of saturation changes and salt precipitation was monitored by means of micro computer tomography (μCT) under sequestration conditions. Changes of absolute permeability and effective CO_2 permeability were monitored via the differential pressure over the core.

It is often argued that, once the formation is dry, chemical rock-fluid interaction will stop as aqueous chemistry is considered [13]. We tested this assumption by injecting SC H_2S into "dry" limestone, as H_2S/limestone is supposed to be a reactive system, at least in the presence of water (unpublished results). By "dry" we mean that the sample was as dry as achievable by extensive dry inert-gas injection under in-situ conditions. The chemical activity under these non-aqueous conditions was investigated by means of online fluid analysis and ex-situ rock analysis.

EXPERIMENTAL SET-UP

The central part of the experiment is the core holder containing the rock sample. The cylindrical rock sample is surrounded by a Viton-based (H-NBR) sleeve, suitable for operation with aggressive fluids such as SC CO_2 and H_2S, and with plungers on both sample cross sections for fluid injection and production. Confinement pressure and sample heating are applied via the sleeve oil, which is heated and cycled through the annular space between the core-holder jacket and sleeve. The jacket (pressure vessel) is made out of x-ray transparent materials allowing in-situ μCT scanning. The experimental geometry is vertical with the SC phases injected from top to bottom.

The unit is equipped with two feed sections: the first section is used to inject and re-circulate true liquids, which allows in-situ saturation of the rock sample and rock/fluid equilibration to prepare the initial state. The second feed section is used for flooding with liquefied gases. This section is equipped with two 0.5-liter ISCO pumps that can be filled with liquid CO_2 and H_2S from liquefied-gas cylinders. The injected fluids can be dynamically mixed and are pre-heated to experimental temperature in the injection lines on their way to the core. The initial fluid properties can be checked by flow meters (density measurement) and by means of online gas-chromatography (GC) bypassing the rock sample.

The produced or bypassed fluids undergo a two step phase separation at high pressure and temperature (high P/T) and at near-ambient conditions (low P/T). At experimental

conditions the liquid phase is separated from the SC phase which mixes dynamically in a nitrogen stream in the high-P/T separation vessel. The liquids are flashed to near ambient conditions to degas and are subsequently sampled, while the gas phases of both separator vessels are led to an online GC analysis via N_2 streams.

CO_2 INJECTION IN BRINE-SATURATED SANDSTONE

Salt precipitation experiments were performed on Berea sandstone with 500 mD permeability and 22% porosity. The samples were embedded in polycarbonate and are small in cross section and volume (∅ 1 cm and 5 cm length) to obtain representative flow rates and to reduce the experimental time to complete dry-out. The mineralogy of the samples was mainly quartz with some K-feldspar, kaolinite, and minor amounts of other clay minerals as determined by eSEM/EDX. The rock samples were pre-saturated with NaCl based high-salinity brine: 20 wt% NaCl and 2 wt% CsCl. The CsCl was added as a contrast agent for CT scanning as its x-ray absorption coefficient is high, leading to a better contrast between the aqueous and the CO_2-rich phases.

We aimed to observe the spatial distribution of the precipitated-salt phase and therefore μCT imaging was the main source of information in this experiment. Computer tomography is based on x-ray absorption determined by material-specific linear attenuation coefficients (μ), which are directly represented as grey values in each voxel of the reconstructed image [14]. For saturation calculations we made use of tabulated mass-absorption coefficients (μ/ρ) [15], measured and calculated fluid densities (ρ) [16] and the density of the solid-salt phase [17,18]. Because of the sensitivity of saturation calculations to the x-ray contrast agent, we measured relative absorption coefficients of CsCl solutions as a function of CsCl concentration. At 2 wt% CsCl, the mass-absorption coefficient is about 1.6 times larger than that of pure water, which was also used to determine the effective photon energy on the basis of listed mass-absorption coefficients [15].

The dry and clean rock sample was mounted into the core holder and subsequently pressurized and heated under N_2 flow to experimental conditions: 45°C/100 bar corresponding to a saline aquifer at 1000 m depth. To quantitatively determine saturations, scans at 100% CO_2 saturation and 100% brine saturation were recorded. For that purpose, nitrogen was displaced by SC CO_2 (miscible displacement) until 100% CO_2 saturation was reached as checked by the density of the produced fluid. Subsequently, the core was slowly depressurized and evacuated to allow brine saturation without trapping of CO_2. The core was saturated with brine and subsequently pressurized. All the scans were taken at experimental temperature and pressure.

During the experiment, dry SC CO_2 was injected at a constant rate into the brine-saturated core. The pump rate was 1 ml/min at 100 bar fluid pressure and 3°C, resulting in an injection rate of about 2.2 ml/min in the SC state (at 45°C). During the first 40 min brine and CO_2 were produced and, in the following period, only a CO_2 rich phase was produced with no further brine production. At that point, substantial drying by evaporation started, with a differential pressure of 150 mbar, decreasing to a final value of 30 mbar after about 8.5 h of CO_2 flooding.

Changes of fluid saturation and/or the rock matrix during the experiment (e.g. due to salt precipitation) change the x-ray contrast and hence the 3D µCT images. The upper right panel of Figure 1 shows the integrated CT-response profiles along the flow direction at different experimental time steps.

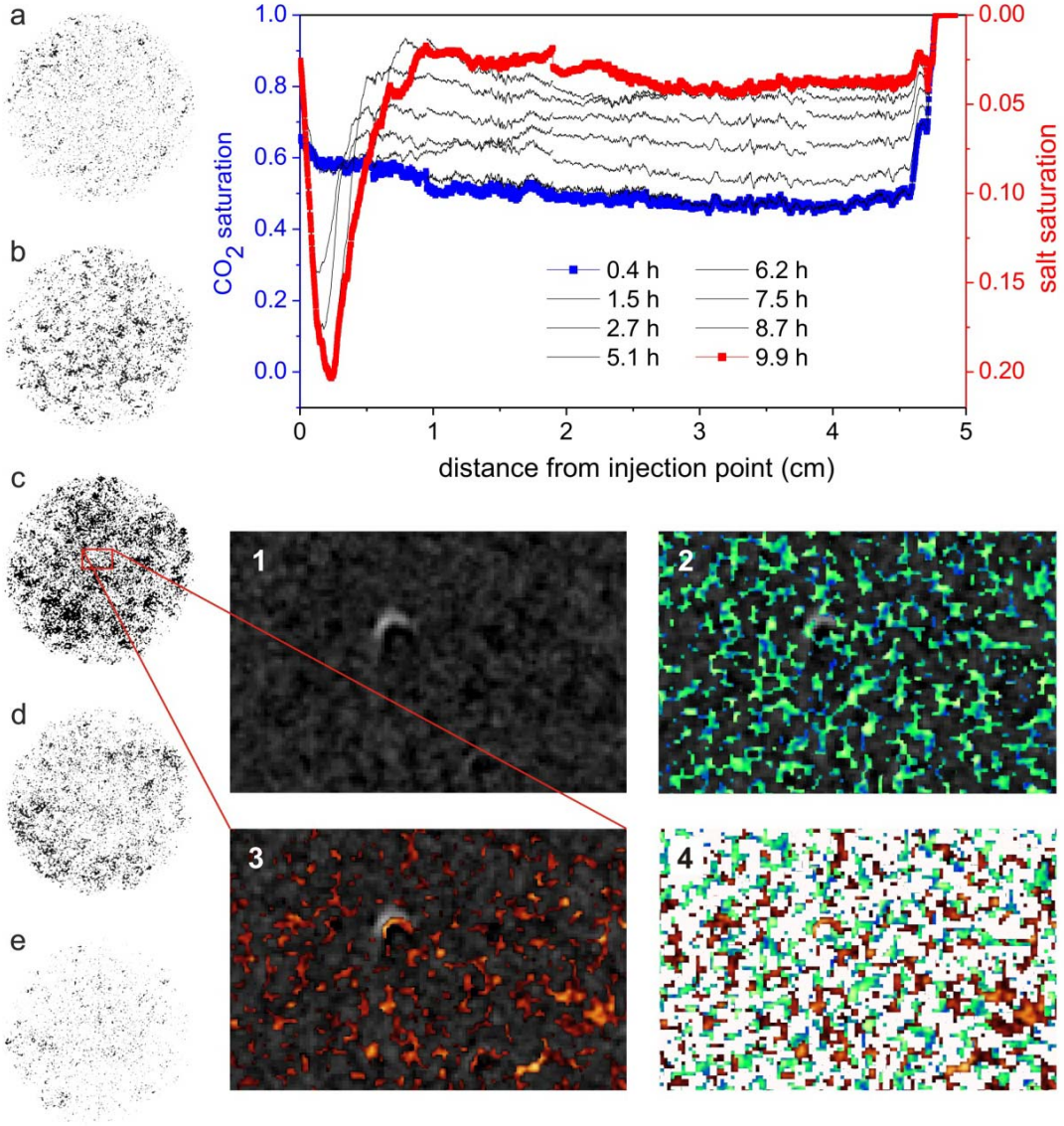

Figure 1: µCT data recorded during the experiment. Upper right panel: time series of normalized difference images (see text) projected onto the vertical sample axis in flow direction. Images on the left: cross sectional difference images showing the solid-salt contribution only; the images a-e are taken in the region of local precipitation between 0 and 0.5 cm in vertical direction (image c at the maximum). Lower right images: cross sectional areas with higher magnification; see text: 1. rock, 2. rock and CO_2 percolation pattern after 0.4 h, 3. rock and precipitated salt after 10 h of CO_2 flooding, 4. superposition of CO_2 percolation pattern and precipitated salt.

The spectra are differences so that the rock matrix is eliminated and the spectra represent the CO_2 saturation with a scale ranging from 100% brine saturation (S_{CO2} = 0) to 100%

CO_2 saturation (S_{CO2} = 1).The scale was calculated from CT profiles $I(t)$ integrated along the flow direction by:

$$\hat{S}_{CO2} = \frac{I_{brine} - I(t)}{I_{brine} - I_{CO2}},$$

where I_{brine} and I_{CO2} represent the density profiles of the 100% saturated reference scans, respectively. The first CT scan was started after 0.4 h of CO_2 flooding. The saturation profile is flat, with an average CO_2 saturation of about 0.5 (black profile). At that time the displacement is still advection dominated. Salt precipitation due to evaporation can be ignored and the system, therefore, is in a two-phase regime (CO_2/brine) for which $\hat{S}_{CO2}$ is a good scale.

Subsequently the x-ray absorption decreases with time, in line with an increase in CO_2 saturation. If salt did not precipitate, flat density profiles could be expected, determined by the advection and evaporation of the brine phase. However, while the lightest component of this experiment (CO_2) is being injected, a dip occurs at a position of about 2.5 mm, corresponding to a density increase - *salt precipitates!* The dip grows for about 9.5 h. After 10 h (red spectrum), the shape of the profile, including all features, does not change further for another 6 h of CO_2-flooding. This is a clear indication that the sample is dry. At that point in time, the rock sample contains solid salt and CO_2 which, again, is a two-phase system. It allows the CT response to be rescaled for the red spectrum (dry state) to solid salt saturation by:

$$\hat{S}_{salt} = \alpha \cdot (1 - \hat{S}_{CO2}), \text{ with } \alpha = \frac{\rho_{brine} \cdot (\mu/\rho)_{brine} - \rho_{CO2} \cdot (\mu/\rho)_{CO2}}{\rho_{salt} \cdot (\mu/\rho)_{salt} - \rho_{CO2} \cdot (\mu/\rho)_{CO2}}.$$

The mean value of solid-salt saturation was determined to be 4.6%, however, locally the saturation is as high as 20%. The mean value of 4.6% corresponds to evaporation of 42% of the total water, consistent with the observation that about 1/2 of the brine remained immobile. From this, the average degree of water saturation of the produced CO_2 has been calculated to be about 40%, using the saturation limit of water in CO_2 [16], the injection rate and the experimental time to dry-out. This results in a length scale in the order of 0.1 m in which evaporation and salt precipitation takes place.

The observed salt accumulation is locally much higher than the salt originally present in the brine of the respective volume. This can only be explained by a capillary driven backflow of brine i.e. salt. Both the length scale of the evaporation zone and the local salt accumulation are evidently controlled by evaporation kinetics, by water advection in both fluid phases and by capillarity as discussed in the next section.

Despite the substantial local porosity reduction, the injectivity is not impaired; the effective permeability ($K \cdot k_{rel}$) of the CO_2-rich phase increased by a factor of 5 from the point of breakthrough to total dry-out. The absolute permeability (K), as measured by dry-CO_2 flooding before and after the experiment, however, decreased by a factor of 4. The increase in effective permeability is likely to be a result of the observed cross-sectional precipitation pattern.

The images on the left side of Figure 1 (images a-e) show the full μCT cross sections (10 mm diameter) across the volume of maximum solid-salt accumulation (0 to 5 mm). The figures range from close to the inlet (a) to about 5 mm into the sample (e) and show

the solid-salt contribution at the point in time when the sample is dry (9.9 h). Conspicuously, the salt precipitates in spots on different length scales, ranging from an mm-scale to a sub-mm or even a micrometer-scale; images with a higher zooming factor are shown in the lower right (images 1 to 4; area of 2.4 mm x 1.6 mm in the vicinity of the precipitation maximum). The images show: (1) an orthogonal slice through the brine saturated rock matrix, (2) the superimposed early CO_2-percolation pattern (after 0.4 h), (3) the precipitated salt phase superimposed on (1) and (4) the precipitated salt superimposed on the early percolation pattern. Both the early CO_2 and solid salt patterns are obtained in a two-phase situation. The images indicate salt precipitation in the vicinity of the percolation pathways, leaving the cross-sectional area of the CO_2-pathways open (hypothesis). This means that there must be capillary-driven cross-sectional water transport from water saturated areas into the high-permeability CO_2 channels in addition to longitudinal water transport.

MODELING LOCAL SALT PRECIPITATION

For an understanding of the fundamental mechanism behind the observed local precipitation, we performed numerical simulations with *Tough2* [19], which is a multiphase/multi-component reservoir simulator. In combination with the fluid property module *ECO2N* which describes the thermodynamics of H_2O/NaCl/CO_2 systems, *Tough2* has been used to model CO_2 injection in saline aquifers [19]. The present experiments were modeled in a vertical 1D geometry using the experimental dimensions. The first grid block was assigned as injector at a constant CO_2 injection rate. The constant pressure boundary condition was realized by setting the volume factor of the last grid block to infinite. The rock properties K, k_{rel} and P_C were derived from experimental data [20].

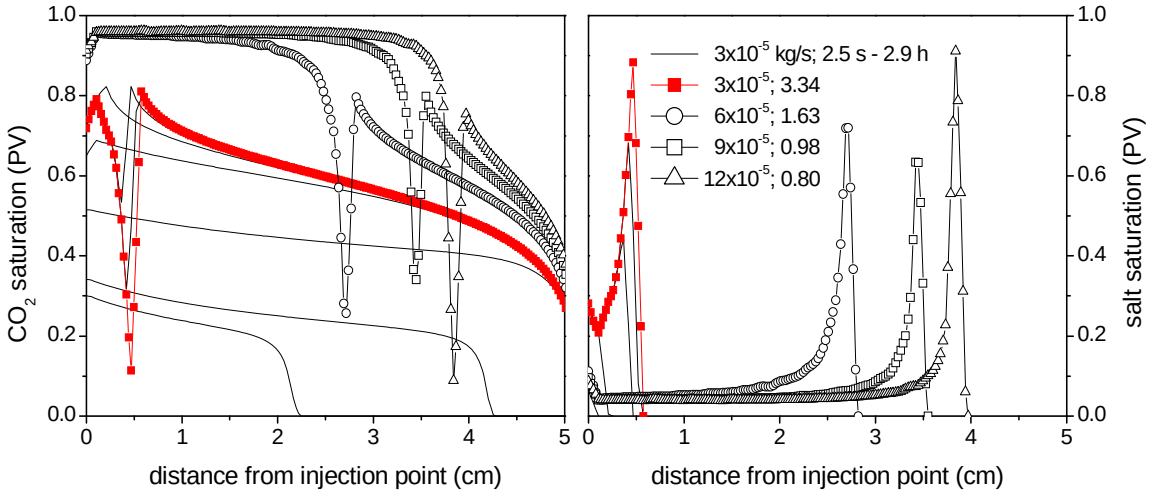

Figure 2: *Tough2* simulations of core-flood experiments. Left panel: CO_2-saturation profiles during CO_2 injection into a brine saturated rock sample at a rate of $3x10^{-5}$ kg/s and at different time steps (lines and closed squares). Also shown are the final states of simulations at higher injection rates (open symbols). Right panel: respective solid-salt saturation profiles.

The left panel of Figure 2 shows longitudinal CO_2 saturation profiles (in direction of injection) simulated with a CO_2 injection rate of $3x10^{-5}$ kg/s for several time steps (black lines). At the given injection rate, the shock front passes the core within seconds, followed by a continuous saturation change after breakthrough. After about 0.3 h, a dip in the gas saturation close to the injection point occurs. This is attributed to a saturation change due to salt precipitation as displayed in the right panel. With advancing time, a precipitation front slowly moves from the injection point downstream, accumulating salt on its way. After 3.3 h of CO_2 flooding, the solid-salt saturation exceeds 0.9 and the simulation stops; in the next time step the salt saturation would reach 1. Permeability changes are not taken into account here, but a blockage of pore space will obviously lead to a blockage of permeability. At the point of blockage, more salt is precipitated than was originally present in the respective brine volume, which requires the transport of salt to the point of dry-out.

In the same panels in Figure 2, simulations at higher injection rates are displayed in their respective final states. At higher injection rates the location of precipitation shifts away from the injection point towards a larger saturation gradient (as determined by the capillary end effect). Apparently, a stronger saturation gradient is needed to reach the condition that leads to local precipitation if the viscous force increases.

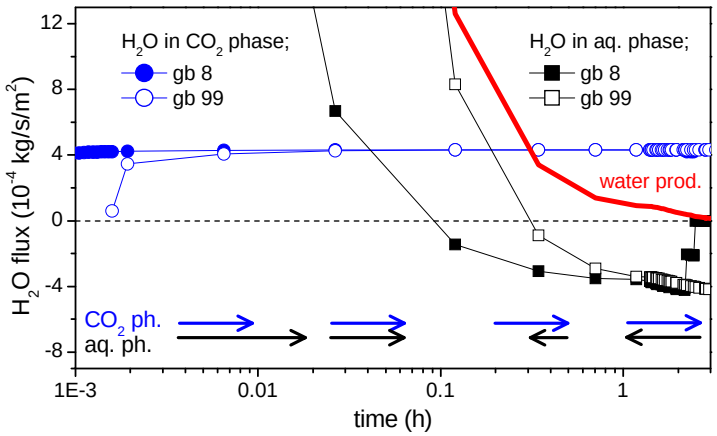

Figure 3: H_2O fluxes in individual grid blocks (gb) as function of time. Squares represent the H_2O flux in the aqueous phase and circles represent the H_2O flux in the CO_2-rich phase due to evaporation and subsequent advection. Note that the aqueous phase changes the flow direction as indicated by the arrows.

More insight into the precipitation mechanism is provided in Figure 3. The effective water fluxes of an individual cell at the point of local precipitation (closed symbols) and at the outlet (open symbols) are plotted against time. The streams are split into water flux in the CO_2-rich phase (blue circles) and in the aqueous phase (black squares). The red line marks the total water flux at the outlet. The water flux in the CO_2-rich phase is determined by the water content and the injection rate. It stays constant over a long period of time, according to the saturation limit. The water transport in the aqueous phase is very intense during the first few seconds but declines rapidly according to the mobility ratio of the phases. The aqueous phase becomes immobile and the water transport is determined by evaporation and subsequent advection in the CO_2-rich phase. After a

certain time, capillary pressure dominates the aqueous-phase transport, leading to a capillary-driven backflow into the zone of evaporation. Backflow, however, allows local salt accumulation beyond the original local salt content in the brine. The point at which the salt precipitates is the point at which the 'evaporation front' no longer moves. At this point, the negative water flux in the brine phase compensates for the positive water flux in the CO_2-rich phase (see Figure 3) and we can formulate a condition for local precipitation to occur if:

$$q_{SC} \cdot \rho_{SC} \cdot X_{H2O,SC} = -q_{aq} \cdot \rho_{aq} \cdot X_{H2O,aq},$$

where q_{SC} and q_{aq} are the volumetric fluxes of the CO_2-rich phase and the aqueous phase, ρ_{SC} and ρ_{aq} are the phase densities and $X_{H2O,SC}$ and $X_{H2O,aq}$ are the mass fractions of water in both phases, respectively.

The simulations demonstrate and explain the effect observed in the experiment. However, there are substantial differences between experiment and simulation. The first difference is the origin of the saturation gradient that drives the capillary backflow. In the simulation, the gradient is dominated by the capillary end-effect and is therefore a property of geometry. In the experiment, however, the end effect is suppressed (as is clear from the μCT profiles) by the evaporation kinetics (not accounted for in *Tough2*/*ToughReact*) and by capillary back flow as a consequence of evaporation. Hence, the saturation gradient that leads to local precipitation is determined by evaporation kinetics, and cannot therefore be modeled quantitatively by *Tough2*/*ToughReact* or any other simulator that does not take evaporation kinetics into account.

Secondly, the brine volume in the experiment is finite and this leads to an underestimation of salt saturation as a result of depletion, as can be shown by simulations with finite sample volume (data is not shown here).

SC-H2S INJECTION IN 'DRY' LIMESTONE

The formation of a dry zone was investigated in the previous experiment by injecting CO_2 into sandstone. However, dry-out is considered not only as a process during CO_2 injection, but in general, in relation to the injection of under-saturated fluids in water-bearing formations. Besides the porosity/permeability reduction as discussed above, a dry-out might also have positive consequences, e.g. chemical stability; reactive transport modeling assumes aqueous chemistry [13] and therefore needs an aqueous phase for chemical activity. We checked this general assumption by injecting SC H_2S into practically dry limestone.

The experiment was performed on limestone (Euville, outcrop) with a permeability of 170 mD and a porosity of 16%. The sample had a diameter of one inch and a length of 9 cm. The mineralogy was mainly calcite (98%) with clay minerals (illite, chlorite and smectite), as determined by eSEM/EDX. The sample had been dried at 90°C in a vacuum oven and was subsequently mounted in the core holder. Once there, it was pressurized by dry nitrogen to 110 bar pore pressure, and heated up to 110°C under a nitrogen flow of about 2 normal liters/h. To eliminate residual moisture, the sample was flooded under these conditions for about 60 h. Only pure nitrogen was detected in the GC signal of the gas produced from the rock sample.

During the experiment, pure H_2S [21] was injected into the sample. The injection rate was 1 ml/min (pump at 3°C), resulting in 2.5 ml/min in the SC state at experimental condition (110°C/110 bar). The experiment was stopped after 3:40 h and a cumulative injection of 189 g H_2S.

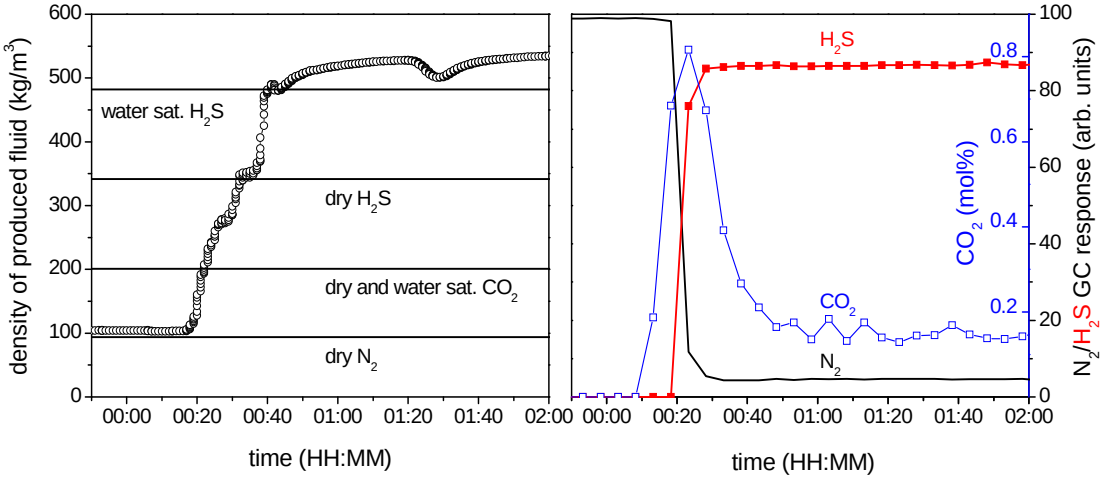

Figure 4: Left panel: density of the produced fluid as function of time. The horizontal lines represent calculated values. Right panel: GC response (integrated peak intensities) in the same time interval. The CO_2 concentration is given in mol% with respect to the H_2S flux after breakthrough.

Figure 4 shows the density of the produced fluid (left panel) and the response of the gas chromatograph (right panel). The fluid density at the start of the experiment is close to 100 kg/m^3, corresponding to the value of nitrogen at the respective experimental condition. With a delay of about 17 min (after starting the pumps), the fluid density starts to increase gradually due to breakthrough of the injected H_2S, until a constant value has been reached after about 1 h. The GC spectra show four peaks, three of which could be identified as N_2, CO_2, and H_2S. The GC response is shown in the right panel of Figure 4, representing the integrated peak intensity as function of time. Up to 00:13, only pure nitrogen was detected. From 00:13 onwards CO_2 appeared in the spectrum, and with a further delay of about 10 min (00:23) a pronounced H_2S signal appeared in the GC response, while the CO_2 peak reached its maximum. About 50 min after the start, the GC signal reaches steady state which continues to the end of the experiment.

The flood front (miscible displacement of gaseous nitrogen by SC H_2S) is reflected in the decreasing N_2 peak and the simultaneously increasing H_2S peak in the GC signal. The offset in the N_2 signal corresponds to the carrier gas from the phase separator to the GC.

The GC data and the density of the produced fluid suggest the following scenario: as SC H_2S is injected into the core it mixes with the N_2, gradually increasing the density of the produced gas. At this very first moment, the H_2S is dilute and converts 100% to CO_2, via a reaction with calcite, as the CO_2 signal appears before the H_2S. After about 32 min, the density reaches a step corresponding to dry H_2S (horizontal lines in the left panel of Figure 4 are calculated densities [16]) and after 5 more min jumps, within a short time interval of two min, to a value corresponding to water saturated H_2S. By definition, 100% water saturation requires the presence of liquid water in the sample. The presence of liquid water suppresses CO_2 production by shielding parts of the water-wet rock surface

with a water film and by dissolving CO_2 in it (water is under-saturated with respect to CO_2); CO_2 production reached a maximum in the vicinity of the flood front, and decreased and finally reached the steady state at a point where reaction (water source) and transport (water sink) have the same rate.
The GC is not sensitive to water, but water production is evident in the measured fluid density. Furthermore, about 1 ml of liquid water was collected in the phase separator after the experiment. This amount of liquid water is compatible with the calculation of water transport in a water-saturated H_2S phase and a decrease of water solubility due to the mixing of the produced fluid with nitrogen in the phase separator [16].
The solubility limit of water in H_2S under experimental conditions has been calculated to be 5.3 mol% [16]. This results in a total water production of 0.24 mol of water during the experiment, corresponding to a total volume of 4.3 ml. Despite ongoing dissolution, the pressure drop over the core increased slightly during the experiment from about 50 to 90 mbar, which is likely to be a relative permeability effect due to water production.
We conclude that water and CO_2 are reaction products of H_2S injected into a limestone. The molar ratio of water and CO_2 is in the order of 30 to 50. Further products have not been identified. The initial reaction is likely to be induced by water but does not take place in an aqueous phase.

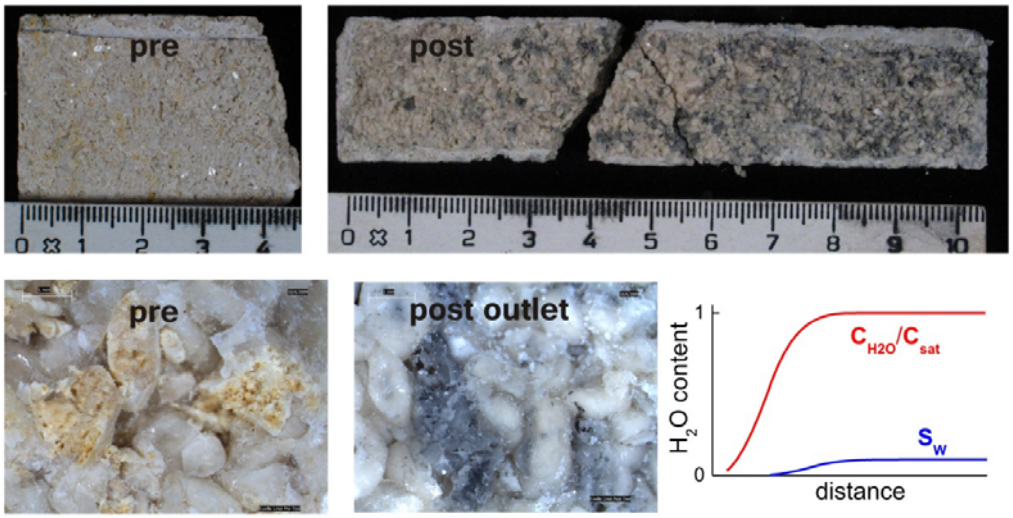

Figure 5: Limestone sample pre and post experiment. The photographs at the top show the initial rock sample (twin sample) and the sample after the experiment (inner part, injection point on the left). The two photographs below are taken through a microscope from the original sample and from the outlet of the exposed sample. The graph in the lower right corner illustrates the mental picture leading to the color gradient as visible after the experiment (upper right photo).

Figure 5 provides a view into the rock sample before and after the experiment. The photographs (top) and the microscopic images (bottom) are taken from a surface, broken along the axis of flow, exposing the central part of the sample. Compared to the light color of the original sample (top left), the exposed sample (top right) shows relatively dark colored areas and a color gradient from the lighter colored inlet (left side) to the darker outlet. The microscopic images show brownish clay minerals from the original

sample that have been converted to blackish minerals that have not yet been identified, but which are likely to be sulfides such as FeS. This is a side reaction that acts as an indicator and provides a qualitative understanding of the core-flood experiment. The graph in the lower right illustrates a mechanism that could lead to the observed profile. The region close to the inlet is kept dry during the experiment because the injected fluid is dry. The water that is produced by the dissolution reaction is transported from the inlet downstream. After a certain distance, the injected H_2S stream is water-saturated and liquid water accumulates beyond that point. According to that picture, the color gradient along the flow axis originates from a qualitative transition from a "dry" (as defined above) and a truly aqueous reaction zone, where the observed side reaction occurs.

CONCLUSION

In conclusion, we investigated two important aspects of dry-zone formation near an injection site due to CO_2 or acid-gas injection. We injected dry SC CO_2 into brine-saturated sandstone and reached complete dry-out. We observed that the capillary-driven backflow of brine can lead to local salt accumulation. The amount of precipitate is potentially much higher than the level of salt originally present in the respective brine volume. Despite the reduction of the absolute permeability by a factor of 4, the effective CO_2 permeability increased during the experiment by a factor of 5 as a consequence of relative permeability and saturation change, suggesting no impairment of injectivity in the present case. This might be attributed to the observed cross-sectional precipitation pattern; salt seems to precipitate in the vicinity of CO_2-flow channels, leaving them essentially open.

The principal mechanism and the condition under which local precipitation occurs have been investigated by numerical simulations, however, we have shown that numerical tools that do not include evaporation as a kinetic approach are not able to quantitatively (nor even qualitatively) describe CO_2 injection on an experimental scale.

Secondly, we investigated the chemical stability of a dry zone. SC H_2S was injected into dry limestone, i.e. in the absence of an aqueous phase. We observed a dissolution reaction producing water and CO_2. A transition from a 'dry' reaction zone to truly aqueous chemistry by accumulating liquid water in the rock sample was observed. Hence, we have demonstrated that a dry zone is not necessarily chemically inert.

ACKNOWLEDGEMENTS

The authors gratefully acknowledge the excellent technical assistance of Mark Hageman and the experimental support teams at Shell Amsterdam and Rijswijk. For valuable discussions and for reading the manuscript we would like to thank Steffen Berg and Jeroen Snippe.

REFERENCES

* Corresponding author; E-mail address: holger.ott@shell.com

1. IPCC Special Report on Carbon Dioxide Capture and Storage, Cambridge University Press, UK, 2005.
2. S. Bachu and W. D. Gunter, Overview of acid-gas injection operations in western Canada, In: *Proceedings of the 7th International Conference on Greenhouse Gas Control Technologies. Volume 1*, Vancouver, BC, September 5-9, 2004.

3. K. Pruess and J. García, Multiphase Flow Dynamics During CO_2 Injection into Saline Aquifers, *Environmental Geology,* Vol. 42, pp. 282 - 295, 2002.
4. R. C. Fuller, J. H. Prevost and M. Piri, Three-Phase Equilibrium and Partitioning Calculations for CO_2 Sequestration in Saline Aquifers, *J. Geophys. Res.,* Vol., 111, 2006.
5. T. Giorgis, M. Carpita and A. Battistelli, 2D Modeling of Salt Precipitation During the Injection of Dry CO_2 in a Depleted Gas Reservoir, *Energy Conv. Managemt.,* Vol. 48, pp. 1816–1826, 2007.
6. S. Hurter, D. Labregere and J. Berge, Simulations for CO_2 Injection Projects with Compositional Simulator, *SPE-108540*, presented at Offshore Europe 2007 conference of the Society of Petroleum Engineers, Aberdeen, Scotland, September 2007.
7. L. André, P. Audigane, M. Azaroual and A. Menjoz, Numerical Modeling of Fluid–rock Chemical Interactions at the Supercritical CO_2–liquid Interface during CO_2 Injection into a Carbonate Reservoir, the Dogger Aquifer (Paris Basin, France), *Energy Conv. Mgmt.,* Vol. 48, No. 6, pp. 1782–1797, 2007.
8. Irina Gaus, Pascal Audigane, Laurent Andre´, Julie Lions, Nicolas Jacquemet, Pierre Durst, Isabelle Czernichowski-Lauriol, Mohamed Azaroual, Geochemical and solute transport modeling for CO_2 storage, what to expect from it?, *International Journal of Greenhouse Gas Control*, 2, 605 – 625, 2008.
9. P. J. Vaughan, D. E. Moore, C. A. Morrow and J. D. Byerlee, Role of Cracks in Progressive Permeability Reduction During Flow of Heated Aqueous Fluid Through Granite, *J. Geophys. Res.*, Vol. 91, No. B7, pp. 7517–7530, 1986.
10. A. Verma and K. Pruess, Thermohydrologic Conditions and Silica Redistribution Near High-Level Nuclear Wastes Emplaced in Saturated Geological Formations, *Journal of Geophysical Res.*, Vol. 93 (B2), pp. 1159-1173, 1988.
11. H. Pape, C. Clauser and J. Iffland, Permeability Prediction Based on Fractal Pore-Space Geometry, *Geophysics,* Vol. 64, No. 5, pp. 1447 - 1460, 1999.
12. T. Xu, Y. Ontoy, P. Molling, N. Spycher, M. Parini and K. Pruess, Reactive Transport Modeling of Injection Well Scaling and Acidizing at Tiwi Field, Philippines, *Geothermics,* Vol. 33, No. 4, pp. 477 - 491, 2004.
13. C. M. Bethke, Geochemical Reaction Modeling, Concepts and Applications, Oxford University Press, New York, Oxford, 1996.
14. S. L. Wellington and H. J. Vinegar, X-Ray Computerized Tomography, *Journal of Petroleum Technology*, August 1987.
15. J. H. Hubbell and S. M. Seltzer, *Tables of X-Ray Mass Attenuation Coefficients and Mass Energy-Absorption Coefficients*; http://www.nist.gov/physlab/data/xraycoef/index.cfm.
16. Fluid densities were calculated with STFlash (Shell Global Solutions, 2003); the obtained densities were compatible with literature data and online-measured fluid densities.
17. The density of the precipitated salt was determined from the densities of the single components (http://www.WebElements.org/); complex solid solutions were not taken into account.
18. The brine contained two salts, NaCl and CsCl, with CsCl more soluble than NaCl. Therefore, the composition of the precipitating salt depends on water advection vs. evaporation, which changes the brine composition to higher CsCl concentrations with time. The CsCl/NaCl ratio of the precipitated phase has been determined by *ToughReact* simulations (data not shown here) to 0.08 (compared to 0.1 in the original brine), corresponding to a scaling factor of $\alpha = 0.2$.
19. K. Pruess and N. Spycher, *ECO2N* – A fluid property module for the *TOUGH2* code for studies of CO_2 storage in saline aquifers, *Energy Conversion and Management* 48, 1761–1767, 2007.
20. P_C was determined by centrifuge measurements using model fluids. The entire data range cannot be described by the available models in *Tough2*, however, a good fit to the data in the relevant saturations range (S_W <0.5) was obtained by the van Genuchten-Mualem model with $\lambda = 0.48$, $S_{lr} = 0.079$, $S_{ls} = 1$, $1/P_0 = 3.5\ 10^{-4}$ and $P_{max} = 10^9$. Also for the relative permeability curves, the van Genuchten model was fitted to the available experimental data; we used the CO_2/brine data on Berea (300 and 430mD) by the Sally-Benson group (http://pangea.stanford.edu/research/bensonlab/relperm/index.html). We focused on the mobility of the aqueous phase (Parameters: $\lambda = 0.7$, $S_{lr} = 0.15$, $S_{ls} = 1$ and $S_{gr} = 10^{-3}$).
21. Purity > 99.9%; C_{CO2} < 100ppm. The water concentration is not specified, but the saturation limit at 20°C/110bar (T_{pump}) is about 5 times lower than at 110°C/110bar - H_2S is heavily under-saturated at experimental condition.